Cell Reports

Article

Reduced inhibition in depression impairs stimulus processing in human cortical microcircuits

Graphical abstract

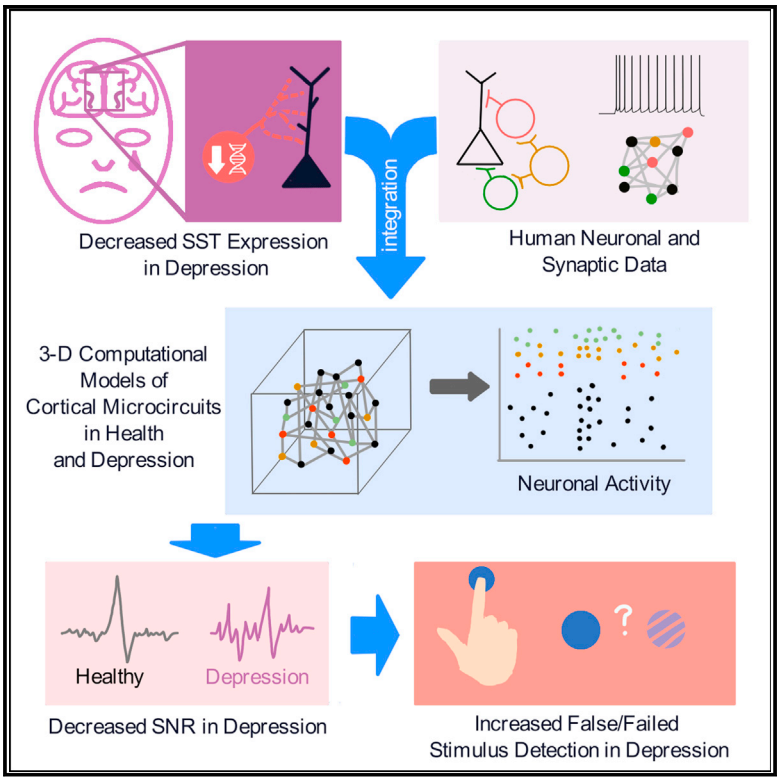

Highlights

- Data-driven models of human cortical neurons, synapses, and microcircuits
- Models of cortical microcircuits in health and depression
- Weaker inhibition in depression increases baseline activity (noise)
- Increased noise leads to increased failed and false detection of stimuli

Authors

Heng Kang Yao, Alexandre Guet-McCreight, Frank Mazza, ..., Taufik A. Valiante, Etienne Sibille, Etay Hay

Correspondence

etay.hay@camh.ca

In brief

Using computational models of human cortical microcircuits that integrate neuronal, synaptic, and gene expression data, Yao et al. show that decreased inhibition from somatostatin interneurons in depression leads to increased noise during information processing and increased false and failed detection of stimuli.

Yao et al., 2022, Cell Reports *38*, 110232
January 11, 2022
https://doi.org/10.1016/j.celrep.2021.110232

CellPress

Cell Reports

CellPress
OPEN ACCESS

Article

Reduced inhibition in depression impairs stimulus processing in human cortical microcircuits

Heng Kang Yao,[1,2,13] Alexandre Guet-McCreight,[1,13] Frank Mazza,[1,2] Homeira Moradi Chameh,[3] Thomas D. Prevot,[4,5] John D. Griffiths,[1,4,6] Shreejoy J. Tripathy,[1,2,4,6] Taufik A. Valiante,[3,6,7,8,9,10,11] Etienne Sibille,[4,5,12] and Etay Hay[1,2,4,14,*]

[1]Krembil Centre for Neuroinformatics, Centre for Addiction and Mental Health, Toronto, ON M5T 1R7, Canada
[2]Department of Physiology, University of Toronto, Toronto, ON M5S 1A1, Canada
[3]Krembil Research Institute, University Health Network, Toronto, ON M5T 0S8, Canada
[4]Department of Psychiatry, University of Toronto, Toronto, ON M5S 1A1, Canada
[5]Campbell Family Mental Health Research Institute, Centre for Addiction and Mental Health, Toronto, ON M5T 1R7, Canada
[6]Institute of Medical Sciences, University of Toronto, Toronto, ON M5S 1A1, Canada
[7]Department of Electrical and Computer Engineering, University of Toronto, Toronto, ON M5S 1A1
[8]Institute of Biomaterials and Biomedical Engineering, University of Toronto, Toronto, ON M5S 1A1, Canada
[9]Department of Surgery, University of Toronto, Toronto, ON M5S 1A1, Canada
[10]Max Planck-University of Toronto Center for Neural Science and Technology, University of Toronto, Toronto, ON M5S 1A1, Canada
[11]Center for Advancing Neurotechnological Innovation to Application, University of Toronto, Toronto, ON M5S 1A1, Canada
[12]Department of Pharmacology & Toxicology, University of Toronto, Toronto, ON M5S 1A1, Canada
[13]These authors contributed equally
[14]Lead contact
*Correspondence: etay.hay@camh.ca
https://doi.org/10.1016/j.celrep.2021.110232

SUMMARY

Cortical processing depends on finely tuned excitatory and inhibitory connections in neuronal microcircuits. Reduced inhibition by somatostatin-expressing interneurons is a key component of altered inhibition associated with treatment-resistant major depressive disorder (depression), which is implicated in cognitive deficits and rumination, but the link remains to be better established mechanistically in humans. Here we test the effect of reduced somatostatin interneuron-mediated inhibition on cortical processing in human neuronal microcircuits using a data-driven computational approach. We integrate human cellular, circuit, and gene expression data to generate detailed models of human cortical microcircuits in health and depression. We simulate microcircuit baseline and response activity and find a reduced signal-to-noise ratio and increased false/failed detection of stimuli due to a higher baseline activity in depression. We thus apply models of human cortical microcircuits to demonstrate mechanistically how reduced inhibition impairs cortical processing in depression, providing quantitative links between altered inhibition and cognitive deficits.

INTRODUCTION

Cortical processing relies on specific interactions between different types of neurons with distinct electrical properties and synaptic connectivity (Gentet et al., 2012; Tremblay et al., 2016). Accordingly, there is increasing evidence that cortical dysfunction involves changes in cellular and microcircuit properties. Altered cortical inhibition is implicated in a variety of brain disorders, such as autism, schizophrenia, and major depressive disorder (depression) (Duman et al., 2019; Fuchs et al., 2017; Levinson et al., 2010; Lewis et al., 2005; Northoff and Sibille, 2014; Prévot and Sibille, 2020). Reduced dendritic inhibition from somatostatin (SST) interneurons is a key component of the altered inhibition that is associated with treatment-resistant depression and several other disorders (Duman et al., 2019; Fee et al., 2021; Fuchs et al., 2017; Lin and Sibille, 2013; Northoff and Sibille, 2014; Prévot and Sibille, 2020; Seney et al., 2015). Recent findings showed significantly lower SST expression by SST interneurons in postmortem cortical tissue from individuals with depression, which indicates a reduction in SST interneuron-mediated inhibition in depression (Seney et al., 2015). Accordingly, silencing SST interneuron inhibition in rodents produces anxiety and depression symptoms, and new pharmacology facilitating SST interneuron inhibition through alpha-5-gamma-aminobutyric-acid-A (α5-GABA$_A$) receptors led to pro-cognitive and antidepressant effects (Fee et al., 2021; Prevot et al., 2019). However, the link between reduced SST interneuron inhibition and cortical deficits remains to be better established mechanistically, particularly in humans.

In the cortex, SST interneurons primarily target the apical dendrites of pyramidal (Pyr) neurons and provide synaptic and extrasynaptic (tonic) inhibition through activation of α5-GABA$_A$ receptors (Ali and Thomson, 2008; Tremblay et al., 2016). SST interneurons mediate lateral inhibition of Pyr neurons through inhibitory disynaptic loops, where facilitating excitation from a Pyr neuron is sufficient for triggering spikes in an SST interneuron

and, consequently, inhibiting neighboring Pyr neurons (Obermayer et al., 2018; Silberberg and Markram, 2007). At the microcircuit level, SST interneurons are involved in maintaining a low baseline activity of Pyr neurons but are largely silent during the early response of the cortical microcircuit to stimuli (Gentet et al., 2012). The role of SST interneurons in baseline activity is further supported by a 2-fold increase in the baseline firing rate of Pyr neurons when SST interneurons are silenced (Gentet et al., 2012).

In line with these findings, a leading hypothesis suggests that reduced SST interneuron inhibition in depression would increase baseline cortical activity (noise) while minimally affecting stimulus response (signal) and, thus, decrease the signal-to-noise ratio (SNR) of cortical processing (Prévot and Sibille, 2020). This is further supported by studies in animal models of depression, where positive allosteric modulation of α5-GABA$_A$ receptors (which are targeted by SST interneurons) led to pro-cognitive effects and recovery from depression symptoms in rodents (Fee et al., 2021; Prevot et al., 2019). However, it remains unclear whether the level of reduced SST interneuron inhibition estimated from gene expression data in human depression would have a significant effect on baseline activity and, thus, on cortical processing. In addition, the effect of reduced SST interneuron inhibition on Pyr neuron baseline and response activity is difficult to predict because of the inter-connectivity between the different neuron types in the microcircuit. Moreover, the implications of reduced inhibition on processing SNR and signal detection in depression remain to be determined to better link the cellular and circuit effects to specific cognitive deficits in depression, such as individuals being less able to identify relevant signals from noise (Prevot et al., 2020) or unable to suppress loops of internal thoughts in rumination (Northoff and Sibille, 2014).

The link between reduced SST interneuron inhibition and depression is supported by pre-clinical animal models (Fee et al., 2021; Fuchs et al., 2017; Prevot et al., 2019), but there is a need for integrative mechanistic studies to assess whether this translates to humans. There are cellular and circuit similarities between rodents and humans (Hodge et al., 2019) (e.g., in the intrinsic firing properties and connectivity patterns of cell types) but also important differences. Human inhibitory synapses from SST and parvalbumin (PV) interneurons onto Pyr neurons are stronger, with lower probability of synaptic failure and larger postsynaptic potential (PSP) amplitude compared with rodents (Komlósi et al., 2012; Molnár et al., 2016; Obermayer et al., 2018). The connection probability between Pyr neurons in human layer 2/3 (L2/3) is also significantly higher than in rodents (Seeman et al., 2018). Furthermore, human Pyr neuron and interneuron morphologies are larger than in rodents, with longer and more complex dendrites allowing more complex signal integration (Gidon et al., 2020; Mohan et al., 2015) and a more compartmentalized apical dendritic tree (Beaulieu-Laroche et al., 2018). Therefore, it is imperative to study the mechanisms of dysfunctional cortical processing in depression in the context of human microcircuits.

Computational models are well suited to bridge this gap because of limitations in monitoring human neuron types and microcircuits *in vivo* and because of the increasing data availability of neuronal and synaptic recordings in healthy human cortical slices resected during surgery, especially from cortical L2/3 (Moradi Chameh et al., 2021; Obermayer et al., 2018; Seeman et al., 2018). These data can be integrated into detailed models of human cortical microcircuits to study human cortical processing mechanistically in health and disease. Available models of human L2/3 neurons have reproduced some of the firing properties (Gouwens et al., 2018) but only partly reproduced the frequency-input relationship. These models were not constrained with sag current properties, which depend on dendritic h current, and, thus, were limited in capturing the dendritic input integration properties of the neurons. In addition, there are currently no models of human synaptic connections and cortical microcircuits. Therefore, there remains a need to integrate the available human electrophysiological data into detailed cortical microcircuit models and their baseline and response activity.

In this study, we tested whether the reduced SST interneuron inhibition estimated from gene expression in depression results in significant changes in the SNR of human cortical processing and in the quality of stimulus detection. Using a computational approach, we integrated human cellular, synaptic, and gene expression data from recent studies to generate detailed models of human cortical L2/3 microcircuits that included the major neuron types with their firing and input integration properties, synaptic models, and connection probabilities. We generated depression microcircuit models by reducing the SST interneuron synaptic and tonic inhibition in the circuit according to gene expression data from recent human studies (Seney et al., 2015). We simulated baseline activity and stimulus response as constrained by previous studies of neuron-type activity profiles to characterize the SNR of cortical processing and the failed/false detection rates of stimuli in health and depression.

RESULTS

We first generated data-driven models of human cortical microcircuits and their baseline and response activity, using human cellular and circuit data whenever available and data from rodents otherwise (Table S1). The process included modeling single neurons to represent each of the four key neuron types, modeling synaptic properties, and modeling microcircuits with the appropriate proportion of the different neuron types and connectivity statistics.

Human cortical L2/3 neuron and synaptic models reproduce experimental properties

We generated single-neuron models of the four major cell types in cortical L2/3, using genetic algorithm optimization, to reproduce their electrical properties as measured in human cortical slices. The features of Pyr neuron model firing in response to depolarizing step currents (e.g. spike rate, height, half-width, and adaptation), the frequency-input curve, and sag voltage in response to hyperpolarizing current steps were all within the range (1–2 SDs) of the experimental population (Figure 1A; Table S2), except for the after-hyperpolarization depth, which was marginal (4 SDs). The passive and active firing features of the SST, PV, and vasoactive intestinal peptide (VIP) interneuron models matched the values of the corresponding human neurons (Figures 1B–1D; Tables S3–S5) and were also within the

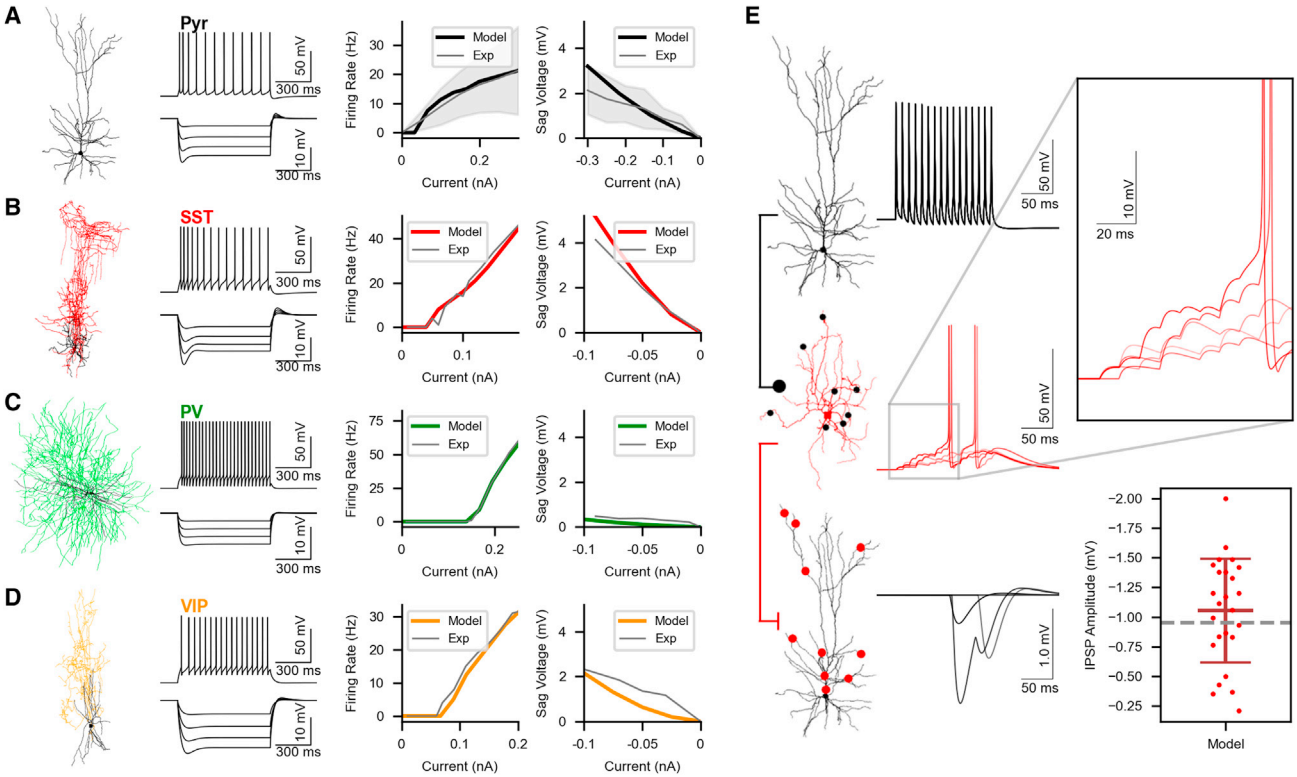

Figure 1. Model human cortical neurons and synaptic connections reproduce experimental properties

(A) Left: reconstructed human L2/3 Pyr neuron morphology. Center: Pyr neuron model response to depolarizing and hyperpolarizing step currents. Right: the firing frequency-input curve and sag voltage-input curve of the Pyr neuron model (black) were within the experimental population range (gray, n = 28 neurons).

(B–D) Same as (A) but for SST (B), PV (C), and VIP (D) interneurons. The firing frequency-input curve and sag voltage-input curve of the interneuron models (SST, PV, and VIP in red, green, and orange, respectively) matched experimental values of the corresponding single neurons (gray).

(E) Simulated voltage traces of a human disynaptic inhibition loop model. A Pyr neuron (top) fired 15 spikes at 100 Hz, and the resulting EPSP summation (inset) in an SST interneuron (center) triggered two spikes, which elicited IPSPs in another Pyr neuron (bottom). The dots on the morphologies indicate synaptic contact locations (black, excitatory; red, inhibitory). The graph at the bottom right shows the simulated IPSP amplitude between SST and Pyr neurons (n = 25 random connections) compared with the experimental value (dashed line; Obermayer et al., 2018).

Data are represented as mean ± SD.

experimental variance of population data from corresponding neurons in rodents (Ma et al., 2006; Prönneke et al., 2015; Zurita et al., 2018). Spike half-width in the PV models was farther from the experimental variance (4.4–4.8 SDs), which is commonly the case because of the fixed kinetics of the underlying channel models (Gouwens et al., 2018; Hay et al., 2011).

Next we generated models of synaptic connections between neuron types. We constrained the connections between Pyr neurons and SST interneurons to reproduce properties of the disynaptic inhibition loop as recorded in human brain slices (Figure 1E). The model synaptic connections from Pyr neurons onto SST interneurons elicited facilitating excitatory PSPs (EPSPs) with amplitudes as seen experimentally (Obermayer et al., 2018) (model, 2.16 ± 1.35 mV; experimental, 2 mV) and were sufficiently strong to trigger 1–2 spikes in the SST interneuron in response to a train of inputs from a single Pyr neuron. The resulting SST interneuron inhibitory PSP (IPSP) amplitudes in a neighboring Pyr neuron agreed with the experimental value (Obermayer et al., 2018) (model, −1.05 ± 0.44 mV; experimental, −0.95 mV). In addition, we constrained the EPSP amplitudes between Pyr neurons and the connections between Pyr and PV neurons to reproduce the experimental values seen in human neurons (Pyr→Pyr model: 0.42 ± 0.37 mV, experimental: 0.42 ± 0.45 mV; Pyr→PV model: 3.29 ± 1.16 mV, experimental: 3.29 ± 1.12 mV; PV→Pyr model: −2.23 ± 1.2 mV, experimental: −2.23 ± 1.0 mV). The remaining types of synapses, primarily involving VIP neurons, were constrained using rodent data because human data were unavailable (Table S7). In addition to synaptic inhibition, we modeled tonic inhibition using voltage-clamp recordings of the tonic current in human Pyr neurons (STAR Methods). We estimated the tonic conductance using the measured difference between tonic inhibition current and when $GABA_A$ receptors were blocked. We reproduced the target tonic inhibition current amplitude with a tonic conductance of 0.938 mS/cm^2 and applied it to all neurons (Scimemi et al., 2006).

Increased baseline activity (noise) in depression microcircuit models

We used the neuron and synaptic connection models to simulate human cortical L2/3 microcircuits of 1,000 neurons with the

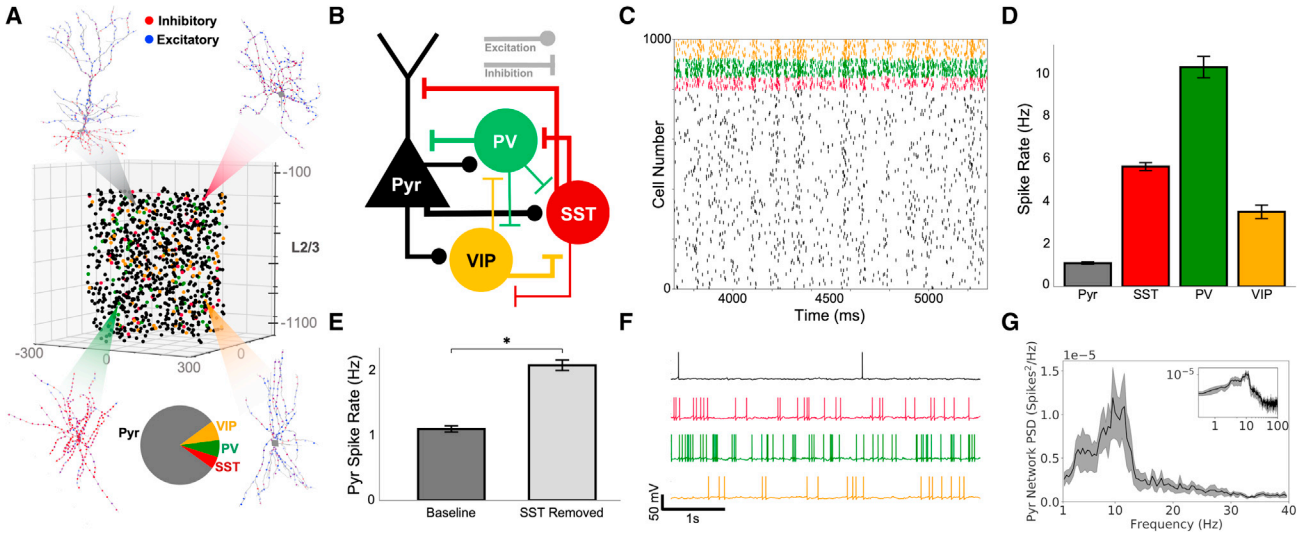

Figure 2. Detailed models of human cortical L2/3 microcircuits reproduce features of intrinsic circuit activity

(A) The model microcircuit is comprised of 1,000 neurons, with the somata distributed in a 500 × 500 × 950 μm^3 volume along L2/3 (250–1,200 μm below the pia). The proportions of the different neuron types were based on the experimental literature (pie chart; Pyr, 80%; SST, 5%; PV, 7%; VIP, 8%). The neurons were modeled with detailed morphologies, as shown in Figure 1, and connected according to the experimental statistics (STAR Methods). The blue and red dots on each morphology denote example excitatory and inhibitory synapses, respectively.

(B) A schematic connectivity diagram highlighting the key connections between different neuron types in the microcircuit.

(C) Example raster plot of spiking in different neurons in the microcircuit, color-coded according to neuron type. Neurons received background excitatory inputs to generate intrinsic circuit activity.

(D) Spike rates in the different neuron types reproduced experimental baseline firing rates (mean ± SD, n = 10 randomized simulated microcircuits).

(E) A significant 2-fold increase in mean Pyr neuron spike rate when SST interneurons were silenced reproduced experimental results (n = 10 microcircuits, paired-sample t test, $p < 0.001$).

(F) Example simulated voltage traces for each neuron type.

(G) Spikes PSD of Pyr neurons, bootstrapped mean, and 95% confidence intervals (n = 10 randomized microcircuits). Inset: PSD in log scale, illustrating the 1/f relationship between power and log frequency.

Data are represented as mean ± SD.

experimental proportions of the different neuron types and their connectivity and column dimensions (Figures 2A and 2B). The neurons received random background excitatory input corresponding to cortical and thalamic drive to enable recurrent activity. We tuned the background excitatory input level and the microcircuit connection probabilities between neuron types to reproduce the baseline firing rates reported previously for the neuron types *in vivo* (Figures 2C, 2D, and 2F). The average firing rate for simulated Pyr neurons was 1.10 ± 0.05 Hz (PV, 10.31 ± 0.50 Hz; SST, 5.64 ± 0.18 Hz; VIP, 3.51 ± 0.32 Hz; n = 10 microcircuits, rates for non-silent neurons as in experiments; STAR Methods). In addition, we constrained the microcircuit to reproduce the effects of SST interneuron silencing, which has been reported previously to result in a doubling of baseline Pyr neuron spike rates (Gentet et al., 2012; Figure 2E; 1.10± 0.05 Hz versus 2.08 ± 0.08 Hz, t test, $p < 0.001$).

The microcircuit models had an emergent property of oscillatory activity, which was not constrained for explicitly, where population spiking oscillated primarily in the theta (4- to 8-Hz) and alpha (8- to 12-Hz) frequency bands and, on average, exhibited peak frequencies around 10 Hz (Figure 2G). The power spectrum density (PSD) plot also exhibited a 1/f relationship between power and log frequency f (Figure 2G, inset). These oscillatory properties closely agree with the oscillations seen in human cortical signals *in vitro* and *in vivo* (Colombo et al., 2019; Florez et al., 2015; Grin-Yatsenko et al., 2009; Halgren et al., 2019), providing validation in support of the models capturing key properties of human cortical L2/3 microcircuits.

We next modeled human depression microcircuits by reducing SST interneuron synaptic and tonic inhibition conductance onto the different neuron types by 40%, according to post-mortem gene expression data in depression (Figures 3A and 3B). We then compared the baseline activity in healthy and depression microcircuits across all neurons of each type. The average baseline firing rate of Pyr neurons was significantly higher in depression microcircuits compared with healthy microcircuits (Figures 3C and 3D; healthy, 0.77 ± 0.05 Hz; depression, 1.20 ± 0.07 Hz; n = 200 randomized microcircuits, t test $p < 0.05$, Cohen's $d = 7.06$). Next we quantified the effect of different levels of SST interneuron inhibition reduction on baseline rates of Pyr neurons by simulating microcircuits with 0%–100% reduction compared with the healthy level. The baseline firing of Pyr neurons increased approximately linearly with reduced SST interneuron inhibition (Figure 3D). Similar increases in firing rates were observed in the interneuron populations of the depression microcircuits compared with healthy microcircuits (Figure 3E; SST, 5.62 ± 0.27 versus 7.53 ± 0.39 Hz; PV, 10.19 ± 0.51 versus 15.99 ± 0.54 Hz; VIP, 3.52 ± 0.37 versus 7.26 ± 0.49 Hz; n = 200,

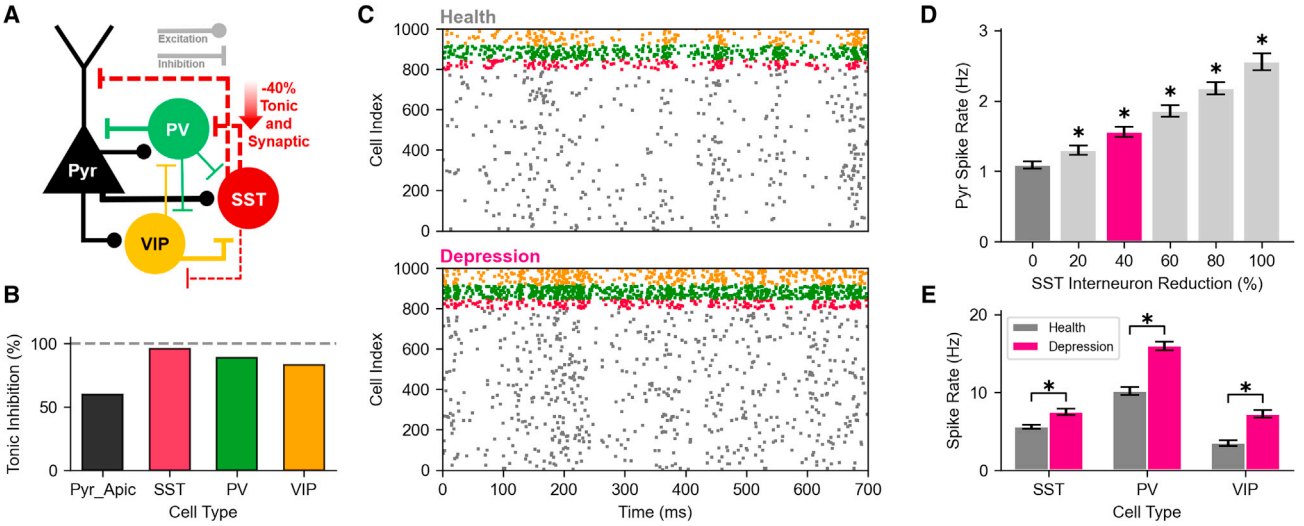

Figure 3. Increased baseline activity (noise) in depression microcircuit models

(A) Depression microcircuits were modeled according to gene expression data, with −40% synaptic and tonic inhibition conductance from SST interneurons onto the other neuron types.

(B) Relative tonic inhibition conductance onto the different neuron types in depression microcircuits compared with healthy microcircuits (dashed line).

(C) Example raster plot of simulated baseline spiking in a healthy microcircuit model (top) and depression microcircuit model (bottom).

(D) Increased intrinsic Pyr neuron firing in depression microcircuit models (n = 200 randomized microcircuits per condition; purple, depression; $p < 0.05$, Cohen's $d = 7.06$; healthy level in dark gray). The relationship between SST interneuron inhibition reduction and baseline Pyr neuron firing rate was approximately linear.

(E) Increased interneuron baseline firing rates in depression microcircuit models ($p < 0.05$).

Data are represented as mean ± SD.

$p < 0.05$ for all). The interneuron rate increase was largest in VIP interneurons (106%) and PV interneurons (57%) and more moderate in SST interneurons (34%). The higher activity in depression microcircuits when no stimulus was given indicated an increased noise level with respect to processing incoming stimuli. To dissect the individual contribution of reducing synaptic versus tonic inhibition, we repeated the simulation with selectively reducing SST interneuron synaptic inhibition or reducing SST interneuron tonic inhibition. We found similar levels of increase in baseline firing rates under each condition (synaptic only, 0.98 ± 0.06 Hz; tonic only, 0.98 ± 0.06 Hz). The effect of the joint synaptic and tonic inhibition reduction was therefore approximately the sum of the separate effects (separate, 1.19 ± 0.08 Hz; joint, 1.20 ± 0.07 Hz; Cohen's $d = 0.13$).

Reduced SNR of cortical processing in human depression microcircuits

To better understand the implications of the increased baseline firing in depression microcircuits, we compared their evoked response activity with that of healthy microcircuits. We modeled a healthy evoked response to a brief stimulus by reproducing the temporal profile and average firing rates in the neuron types as measured in cortical L2/3 *in vivo* (in rodents). VIP and PV interneurons were stimulated earliest and, consequently, silenced SST interneurons. Pyr neurons were stimulated shortly thereafter and responded with brief peak firing followed by a sustained lower response rate, although still above baseline, that lasted ~100 ms (Figures 4A and 4B). Over the 5- to 55-ms window after the stimulus, Pyr neurons fired at 2.49 ± 0.61 Hz on average (n = 200 randomized microcircuits). We then applied this stimulus paradigm to the depression microcircuits and found no significant change in average Pyr response rate (Figure 4C ; 2.52± 0.47 Hz, Cohen's $d = 0.06$). The evoked response of interneurons was similar in healthy and depression microcircuits as well (Figure 4I; SST: 2.74 ± 1.34 versus 3.21 ± 1.55 Hz, Cohen's $d = 0.32$; PV: 30.62 ± 4.79 versus 32.06 ± 3.43 Hz, $d = 0.35$; VIP: 32.88 ± 2.92 versus 34.94 ± 2.52 Hz, $d = 0.76$).

We calculated the overall SNR in the healthy and depression microcircuits as the ratio of the response activity (signal) and baseline activity (noise) across the Pyr neuronal population and found significantly (>50%) reduced SNR in depression microcircuits (Figure 4D; health, 3.26 ± 0.80; depression, 2.09 ± 0.39, $p < 0.05$; Cohen's $d = 1.86$). The reduction in SNR was similarly significant when examining only the stimulated Pyr neurons (Figure 4E; health, 22.67 ± 3.78; depression, 14.75 ± 2.10; $p < 0.05$, Cohen's $d = 2.59$). Reducing SST interneuron synaptic or tonic inhibition separately had a similar effect on SNR (synaptic only, 2.56 ± 0.57; tonic only, 2.65 ± 0.57). The effect of the joint synaptic and tonic inhibition reductions was therefore approximately the sum of the separate effects (separate, 1.95 ± 0.80; joint, 2.09 ± 0.39; Cohen's $d = 0.22$). To further investigate the effect of reduced SNR on cortical processing, we determined the corresponding change in false/failed signal detection rates. We calculated the distribution of spike rates of all Pyr neurons in 50-ms windows before and after stimulus to calculate the probability of false positive/negative errors in stimulus processing (Figures 4F and 4G). We found a significant increase, more than double, in the false detection rates (health, 3.76% ± 1.60 %; depression, 10.07% ± 3.02 %; $p < 0.05$, Cohen's $d = 2.61$) and failed detection rates (health, 2.40% ± 0.67 %; depression,

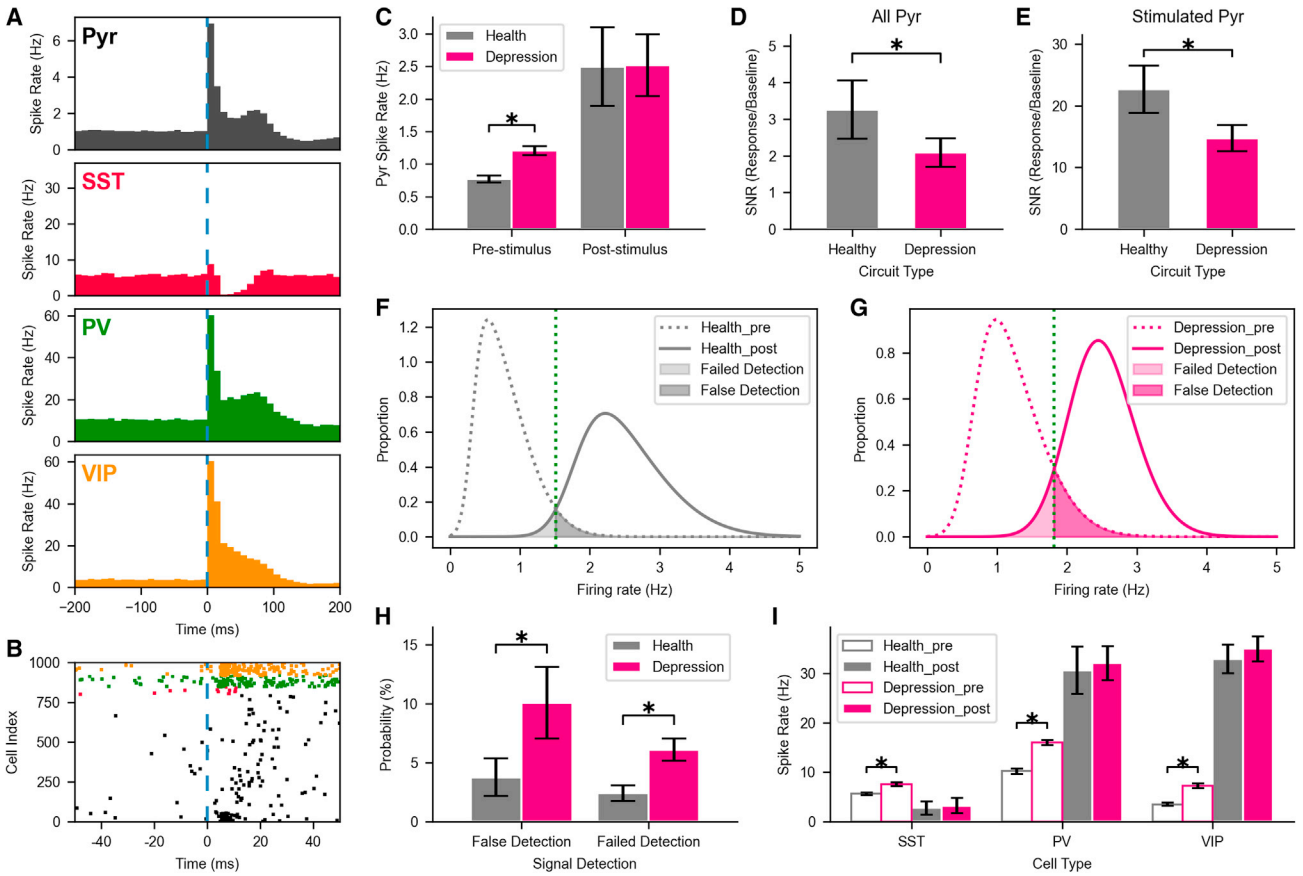

Figure 4. Decreased cortical SNR and impaired stimulus detection in depression microcircuit models

(A) Average peristimulus time histogram (n = 200 randomized microcircuits) of a simulated response to a thalamic stimulus in healthy microcircuits reproduces response firing rates and profiles recorded in the different neuron types in awake rodents. A dashed line denotes the stimulus time.

(B) Example raster plot of simulated spike response in a healthy microcircuit model.

(C) Baseline Pyr neuron firing rates in depression microcircuits were significantly higher than in healthy microcircuits ($p < 0.05$, Cohen's $d = 7.06$), but response rates were similar (Cohen's $d = 0.06$).

(D) Decreased SNR (ratio of response versus baseline Pyr neuron firing rates) in depression microcircuits.

(E) Same as (D) but for the stimulated Pyr neurons only.

(F) Distribution of pre- and post- stimulus firing rates in 50-ms windows in healthy microcircuits (n = 1,950 windows × 200 microcircuits pre-stimulus, n = 200 windows post-stimulus). The vertical dotted line denotes the decision threshold of signal detection (STAR Methods).

(G) Same as (F) but for depression microcircuits.

(H) Increased probability of false detection and failed detection in depression versus healthy microcircuits.

(I) Baseline and response firing rates in interneurons in healthy and depression microcircuits.

*$p < 0.05$. Data are represented as mean ± SD.

6.01% ± 0.94%; $p < 0.05$, Cohen's $d = 4.42$) in depression (Figure 4H). Reducing SST interneuron synaptic or tonic inhibition separately had a similar effect on the false detection rate (synaptic only, 6.46% ± 2.23 %; tonic only, 5.58% ± 1.94 %) and failed detection rate (synaptic only, 4.10% ± 0.88%; tonic only, 4.34% ± 0.85%). The effect of the joint synaptic and tonic reductions was therefore approximately the sum of the separate effects on false detection (separate, 8.28% ± 2.96 %; joint, 10.07% ± 3.02 %; Cohen's $d = 0.60$) and failed detection (separate, 6.04% ± 1.22% joint, 6.01% ± 0.94%; Cohen's $d = 0.03$).

To determine the effect of SST interneuron inhibition reduction on processing of top-down inputs, we repeated our previous analysis but with apical dendritic stimulation (corresponding to cortico-cortical inputs). Similarly to basal dendritic stimulation, there was no significant change in response rates (Figure 5B; healthy, 2.96 ± 0.71 Hz; depression, 2.86 ± 0.56 Hz; Cohen's $d = 0.16$), and there was a similar level of decrease in SNR (Figure 5C; health, 3.88 ± 0.95; depression, 2.39 ± 0.49; $p < 0.05$; Cohen's $d = 1.97$) and increase in false detection rate (Figure 5D; health, 2.09% ± 0.79%; depression, 6.21% ± 2.20%, $p < 0.05$; Cohen's $d = 2.49$) and failed detection rate (Figure 5D; health, 2.54% ± 0.62 %; depression, 4.73% ± 0.90%; $p < 0.05$; Cohen's $d = 2.83$).

To systematically assess the effect of different levels of SST interneuron inhibition reduction on stimulus processing, we simulated microcircuits with 0%–100% reduction compared with the healthy level. The SNR decreased with the level of SST interneuron inhibition reduction (Figure 6A; 0%, 3.26 ± 0.80; 40%,

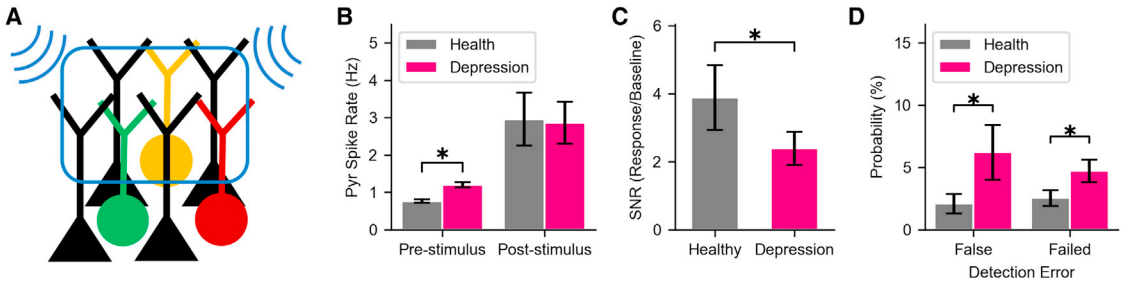

Figure 5. Decreased SNR and increased detection errors in processing top-down inputs

(A) Schematic of apical dendrite stimulation.

(B) Baseline Pyr neuron firing rates in depression microcircuits were significantly higher than in healthy microcircuits, but response rates were similar.

(C) Decreased SNR (ratio of response versus baseline Pyr neuron firing rates) in depression microcircuits.

(D) Increased probability of false detection and failed detection in depression versus healthy microcircuits.

*$p < 0.05$. Data are represented as mean ± SD.

2.09 ± 0.39; 100%, 1.30 ± 0.27), with a sharper decrease up to the reduction level estimated in depression (40%) and a more moderate change beyond that level. Interestingly, the rate of false signal detection increased nonlinearly with the level of inhibition reduction (Figure 6B). There was an effect threshold around the level of reduction estimated in depression, with a negligible change for a smaller reduction (0%, 3.76% ± 1.60%; 20%, 4.94% ± 1.95%; Cohen's $d = 0.66$) and a sharper increase at the depression level and beyond (40%: 10.07% ± 3.02%, $p < 0.05$, Cohen's $d = 2.61$; 100%: 40.07% ± 6.70%, $p < 0.05$, Cohen's $d = 7.45$). A similar nonlinear increase and threshold effect were observed for failed detection rates (Figure 6C; 0%: 2.40% ± 0.67%; 20%: 2.21% ± 0.61%, Cohen's $d = -0.30$; 40%: 6.09% ± 0.94%, $p < 0.05$, Cohen's $d = 4.5$; 100%: 15.44% ± 3.27%, $p < 0.05$, Cohen's $d = 5.5$).

DISCUSSION

This study determined the implications of reduced inhibition in depression on cortical processing in microcircuits, using detailed models of human cortical L2/3 microcircuits that integrated human cellular, circuit, and gene expression data in health and depression. Our simulations of microcircuit response and baseline activity showed that the reduced SST interneuron inhibition in depression estimated by gene expression resulted in a significantly decreased SNR of cortical processing and increased failed/false signal detection rates. Our results provide mechanistic validation for a leading hypothesis of reduced SST interneuron inhibition as a pathological mechanism for dysfunctional processing in depression. This lends support to establishing SST interneuron inhibition as a target mechanism for new pharmacology for treating depression. Furthermore, our results make testable quantitative predictions about the correspondence between different degrees of reduced SST interneuron inhibition and the resulting cognitive deficits that are relevant to symptoms such as rumination and impaired signal detection, which may serve to improve subtyping of depression for better diagnosis, treatment, and drug monitoring in the future.

The reduced SNR and signal detection quality we found in the depression microcircuit models agrees with previous studies that showed deficits in depression in a variety of tasks involving sensory processing, resulting in impaired detection and decision-making (Huang et al., 2017; Koetsier et al., 2002; Tsourtos et al., 2002). Our results may also underlie the inability to break internal loops of thought in rumination symptoms (Northoff and Sibille, 2014). The increase in failed detection in our depression microcircuit models was of a level similar to a previous study involving a visual attention task (Koetsier et al., 2002), and this study similarly found a larger increase in false detection rate compared with the failed detection rate in depression. Other studies that used the paced visual serial addition test and inspection time test found that individuals with depression had slower visual processing speeds and made more calculation errors compared with healthy controls (Khanahmadi et al., 2013; Tsourtos et al., 2002). Individuals with depression have also been shown to perform worse on visual processing tasks such as the Stroop color and word test and in visual surround motion suppression (Den Hartog et al., 2003; Song et al., 2021). Our demonstration of similar effects on cortical processing of apical (cortico-cortical) inputs and the canonical nature of the cortical microcircuitry (Douglas and Martin, 2004) also generalize the implications of our results to higher-order deficits (Taylor Tavares et al., 2007), an important topic that can be explored carefully in future studies. The relationship between dysfunctional microcircuit processing and reduction of SST interneuron inhibition we quantified may serve as a biomarker for diagnosing depression type and severity (McDermott and Ebmeier, 2009). Future studies should examine how the relationship between reduced SST interneuron inhibition and processing is affected by a disruption in neuromodulation by serotonin and acetylcholine, which is implicated in depression (Blier and El Mansari, 2013; Lee et al., 2010; Philip et al., 2010). The link between altered inhibition and brain deficits is further supported by studies of other psychiatric disorders (Marín, 2012). A previous study of the effect of disinhibition in schizophrenia showed a non-linear effect with false signal detection (Murray et al., 2014), similar to what we found. Although additional inhibitory mechanisms may be involved (e.g., PV interneuron dysfunction in schizophrenia; Hashimoto et al., 2003), this similarity may account for common symptoms relating to mood and processing deficits across different disorders (Sibille, 2017).

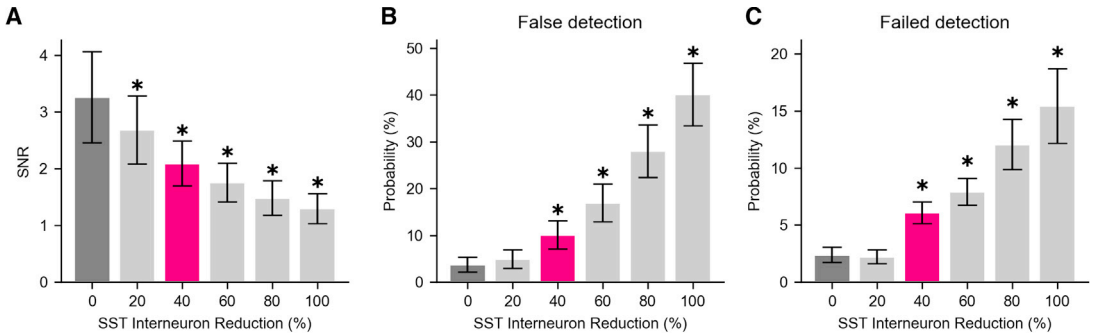

Figure 6. Effect of different levels of reduced SST interneuron inhibition on SNR and signal detection

(A–C) SNR(A), false signal detection rates (B), and failed signal detection rates (C) at different levels of SST interneuron inhibition reduction. *$p < 0.05$ and a large effect size. Data are represented as mean ± SD.

The increased baseline firing rate across cell types in depression microcircuits ultimately resulted from the net effect of different circuit interactions after reducing SST interneuron inhibition, but a few contributing factors can be delineated. The increased Pyr neuron firing led to an increase in interneuron firing rates, and the differences in rate change in different interneuron types would arise partly from the differences in synaptic and tonic inhibition reduction from SST interneurons. In addition, the lower level of rate change in SST interneurons would result from being inhibited further by increased inhibition from VIP and PV interneurons. The new excitation/inhibition balance in depression microcircuits would be restored by increased inhibition from PV interneurons (Xue et al., 2014) but also by the remaining inhibition from SST interneurons. Last, increased activity in VIP interneurons would keep the microcircuit from being overinhibited by PV and SST interneurons.

The effect of synaptic versus tonic inhibition reduction on cortical processing was similar, and these results are informative for pharmacology treatments that target SST interneuron inhibition. Recent studies enhanced α5-$GABA_A$ receptor function through positive-allosteric modulators to improve SST interneuron signaling, which led to pro-cognitive and anxiolytic effects (Piantadosi et al., 2016; Prevot et al., 2020). However, the particular effects of these modulators on cortical circuits are still uncharacterized because of the complex interactions between cell types and differential expression of α5-$GABA_A$ receptors in Pyr, SST, and PV neurons (Davenport et al., 2021; Hu et al., 2018). Our simulations suggest that reduced synaptic versus tonic inhibition contribute similarly to the deficits, implying that both types of inhibition need to be rescued. Therefore, α5-$GABA_A$ receptors, which are localized synaptically and extrasynaptically, serve as good treatment targets (Caraiscos et al., 2004; Davenport et al., 2021). Inhibition of VIP interneurons may be another treatment target because their disproportional increase in firing rate would further exacerbate the reduced contribution of SST interneurons. Our models can serve to test novel treatments systematically *in silico* and also further optimize and discover new treatment targets.

Although our study focused on systematic characterization of inhibition effects, future studies may also expand the analysis to include excitatory dysfunction in depression; e.g., because of synaptic loss (Banasr et al., 2011). Our models of depression examined the implication of reduced inhibition at the microcircuit scale, but future studies could explore the implications for multiregional processing in depression by modeling and stimulating several detailed microcircuits corresponding to the different relevant brain areas and their interactions (Koenigs and Grafman, 2009). Multiregional simulations will help distinguish the similarities and differences of SST interneuron inhibition effects in various neurological disorders where these interneurons are implicated (Lin and Sibille, 2013; Prevot et al., 2020). Multiregional processing simulations will also enable examination of the implications for later stages of the cortical response, where SST interneurons may provide feedback inhibition to reduce excitation when stimuli are similar to contextual surroundings (Keller et al., 2020) or serve to shorten response duration (Yu et al., 2019). Pathologically reduced inhibition in such cases may result in prolonged response time and, thus, slower processing of subsequent stimuli (McDermott and Ebmeier, 2009).

We developed models of human cortical microcircuits to study depression in the context of the human cortex. We were able to improve existing models of human L2/3 neurons to better reproduce the firing frequency-input relationship and the sag voltage, capturing important input integration properties of neurons within the microcircuit. Further improvements of our models can include dendritic ion channels mediating backpropagating action potentials and calcium spikes, which have been well characterized in rodents (Hay et al., 2011). These dendritic properties still remain to be better characterized in humans, but recent studies suggest that calcium spikes may play a role in mediating nonlinear processing in human Pyr neurons (Gidon et al., 2020). However, our microcircuit models are still capable of N-methyl-D-aspartate (NMDA) nonlinearities, which play an important role in the cortical microcircuit (Hay and Segev, 2015). Further refinement of the models would constrain the connectivity between neuron types in the human cortex, which is largely unavailable at present but expected to become available in the near future (Peng et al., 2019). Nevertheless, the model spike oscillations in theta and alpha frequency bands and the 1/f relationship between power and log frequency agree with the oscillations seen experimentally in human cortical signals (Colombo et al., 2019; Florez et al., 2015; Grin-Yatsenko et al., 2009; Halgren et al., 2019) and serve as validation in support of the models capturing key properties of human cortical L2/3 microcircuits.

As human data from other cortical layers become more available, future directions should examine the implication of reduced SST interneuron inhibition in depression for signal propagation across layers (Harris et al., 2019). Future studies should investigate the effects we found differ in rodent microcircuit models, smaller neurons and weaker synapses, to better establish the preclinical relevance of the rodent animal model of depression. Because of the abovementioned species similarities in neuron types and circuit motifs, we expect the results to largely hold for rodent microcircuits as well, although with possible nuanced differences regarding the extent and magnitude of the effects. Our detailed models of healthy microcircuits can further serve to study the cellular and circuit mechanisms of other neurological disorders, such as schizophrenia and epilepsy. Furthermore, our models are implemented in LFPy (Hagen et al., 2018) and thus can be used to study the associated electroencephalography signals and local field potentials from our depression microcircuit models to identify biomarkers for improving diagnosis and monitoring (Mäki-Marttunen et al., 2019).

Limitations of the study

We have applied gene expression data to estimate a reduction in the strength (conductance) of inhibitory connections from SST interneurons (Seney et al., 2015). Although the link between gene expression and cellular function is not trivial, a few factors support our framework. SST receptors are colocalized with GABA receptors, and SST is co-released with GABA and strengthens GABA effects through pre- and postsynaptic mechanisms (Martel et al., 2012). Studies have shown that mice lacking SST peptides have altered GABAergic genes in SST neurons that are consistent with reduced GABA function of these cells (Lin and Sibille, 2015). SST administration has also been shown to have antidepressant effects, and reducing GABA in SST interneurons has been shown to produce anxiety behavior (Engin et al., 2008; Miyata et al., 2019). We thus applied the reduction in SST as a reduced GABAergic inhibitory conductance. The change in gene expression may alternatively reflect a reduced number of synapses (Kang et al., 2012), but the net inhibition decrease in either case would be largely similar. A comparison between conductance decrease and synaptic loss will be interesting to investigate in future studies.

We modeled tonic inhibition as a steady-state inhibitory current that is independent of interneuron firing rates, using currently available models. Although tonic inhibition depends on the interneuron firing rate in addition to GABA release per synaptic event, the rate dependence remains to be characterized experimentally and modeled, and the timescale is often long enough for tonic inhibition to be considered more steady-state inhibition (Bright and Smart, 2013). Our simulations therefore tested the effects of reduced tonic inhibition directly because of reduced synaptic inhibition and GABA release per synaptic event, together with the rate-dependent effects of reduced synaptic inhibition itself. Rate dependence of tonic inhibition effects can refine our results when data and models become available.

Our microcircuit models were constrained with circuit data from different regions because of availability but aimed primarily at representing a canonical cortical microcircuit and response to a brief stimulus. Although different regions, such as sensory and association regions, have some differences in wiring and function when considering all six layers of the cortex, the canonical L2/3 microcircuitry and the response to a brief stimulus are mostly similar across regions (Douglas and Martin, 2004).

We examined the effect of SST interneuron inhibition on cortical processing using the response rate profile in the different neuron types based on available somatosensory studies in rodents because of the lack of similar data in humans. The relevance of rodent response data is supported by the important similarities between the rodent and human cortex in terms of ion channel mechanisms, neuron types, and microcircuit connection motifs such as the SST interneuron inhibitory disynaptic loop (Laubach et al., 2018; Obermayer et al., 2018; Silberberg and Markram, 2007).

STAR★METHODS

Detailed methods are provided in the online version of this paper and include the following:

- KEY RESOURCES TABLE
- RESOURCE AVAILABILITY
  - Lead contact
  - Materials availability
  - Data and code availability
- EXPERIMENTAL MODEL AND SUBJECT DETAILS
- METHOD DETAILS
  - Human L2/3 microcircuit models
  - Neuron models
  - Synaptic connectivity models
  - Tonic inhibition recordings data
  - Tonic inhibition models
  - Modelling microcircuit baseline and response activity
  - Spikes PSD
  - Human depression microcircuit models
  - False/failed signal detection rates
- QUANTIFICATION AND STATISTICAL ANALYSIS

SUPPLEMENTAL INFORMATION

Supplemental information can be found online at https://doi.org/10.1016/j.celrep.2021.110232.

ACKNOWLEDGEMENTS

H.K.Y., A.G.-M., F.M., and E.H. thank the Krembil Foundation for funding support. H.K.Y. and E.H. were also supported by a stipend award from the Department of Physiology at University of Toronto. S.J.T. and T.A.V. are also thankful for generous support from the CAMH Discovery Fund and Kavli Foundation.

AUTHOR CONTRIBUTIONS

Conception, H.K.Y., E.H., E.S., T.A.V., and T.D.P.; methodology, H.K.Y., A.G.-M., E.H., H.M.C., and T.A.V.; software, H.K.Y., A.G.-M., F.M., and E.H.; formal analysis, H.K.Y., A.G.-M., H.M.C., S.J.T., and E.H.; investigation, H.K.Y., A.G.-M., E.H., H.M.C., and T.A.V.; resources, E.H., H.M.C., and T.A.V.; data curation, H.K.Y., A.G.-M., H.M.C., and S.J.T.; writing – original draft, H.K.Y., A.G.-M., and E.H.; writing – review & editing, H.K.Y., A.G.-M., E.H., T.A.V., E.S., T.D.P., H.M.C., F.M., S.J.T., and J.D.G.; visualization, H.K.Y., A.G.-M., and E.H.; supervision, E.H., E.S., T.A.V., and J.D.G.; project

administration, E.H., E.S., and T.A.V.; funding acquisition, E.H., E.S., and T.A.V.

DECLARATION OF INTERESTS

The authors declare no competing interests.

Received: April 9, 2021
Revised: October 7, 2021
Accepted: December 16, 2021
Published: January 11, 2022

REFERENCES

Ali, A.B., and Thomson, A.M. (2008). Synaptic alpha 5 subunit-containing GABAA receptors mediate IPSPs elicited by dendrite-preferring cells in rat neocortex. Cereb. Cortex. *18*, 1260–1271.

Allen Institute for Brain Science (2010). Allen human brain atlas.human.brain-map.org.

Asgari, A., Semnanian, S., Atapour, N., Shojaei, A., Moradi-Chameh, H., Ghafouri, S., Sheibani, V., and Mirnajafi-Zadeh, J. (2016). Low-frequency electrical stimulation enhances the effectiveness of phenobarbital on GABAergic currents in hippocampal slices of kindled rats. Neuroscience *330*, 26–38.

Banasr, M., Dwyer, J.M., and Duman, R.S. (2011). Cell atrophy and loss in depression: reversal by antidepressant treatment. Curr. Opin. Cell Biol. *23*, 730–737.

Beaulieu-Laroche, L., Toloza, E.H.S., van der Goes, M.-S., Lafourcade, M., Barnagian, D., Williams, Z.M., Eskandar, E.N., Frosch, M.P., Cash, S.S., and Harnett, M.T. (2018). Enhanced dendritic compartmentalization in human cortical neurons. Cell *175*, 643–651.e14.

Blier, P., and El Mansari, M. (2013). Serotonin and beyond: therapeutics for major depression. Philos. Trans. R. Soc. B Biol. Sci. *368*, 20120536.

Bright, D., and Smart, T. (2013). Methods for recording and measuring tonic GABAA receptor-mediated inhibition. Front. Neural Circuits *7*, 193.

Bryson, A., Hatch, R.J., Zandt, B.-J., Rossert, C., Berkovic, S.F., Reid, C.A., Grayden, D.B., Hill, S.L., and Petrou, S. (2020). GABA-mediated tonic inhibition differentially modulates gain in functional subtypes of cortical interneurons. Proc Natl Acad Sci U S A *117*, 3192–3202.

Caraiscos, V.B., Elliott, E.M., You-Ten, K.E., Cheng, V.Y., Belelli, D., Newell, J.G., Jackson, M.F., Lambert, J.J., Rosahl, T.W., Wafford, K.A., et al. (2004). Tonic inhibition in mouse hippocampal CA1 pyramidal neurons is mediated by alpha5 subunit-containing gamma-aminobutyric acid type A receptors. Proc. Natl. Acad. Sci. U S A *101*, 3662–3667.

Carnevale, N.T., and Hines, M.L. (2006). The NEURON Book (Cambridge University Press).

Colombo, M.A., Napolitani, M., Boly, M., Gosseries, O., Casarotto, S., Rosanova, M., Brichant, J.-F., Boveroux, P., Rex, S., Laureys, S., et al. (2019). The spectral exponent of the resting EEG indexes the presence of consciousness during unresponsiveness induced by propofol, xenon, and ketamine. Neuroimage *189*, 631–644.

Davenport, C.M., Rajappa, R., Katchan, L., Taylor, C.R., Tsai, M.-C., Smith, C.M., de Jong, J.W., Arnold, D.B., Lammel, S., and Kramer, R.H. (2021). Relocation of an extrasynaptic GABAA receptor to inhibitory synapses freezes excitatory synaptic strength and preserves memory. Neuron *109*, 123–134.e4.

Destexhe, A., Rudolph, M., Fellous, J.M., and Sejnowski, T.J. (2001). Fluctuating synaptic conductances recreate in vivo-like activity in neocortical neurons. Neuroscience *107*, 13–24.

Douglas, R.J., and Martin, K.A.C. (2004). Neuronal circuits of the neocortex. Annu. Rev. Neurosci. *27*, 419–451.

Duman, R.S., Sanacora, G., and Krystal, J.H. (2019). Altered connectivity in depression: GABA and glutamate neurotransmitter deficits and reversal by novel treatments. Neuron *102*, 75–90.

Engin, E., Stellbrink, J., Treit, D., and Dickson, C.T. (2008). Anxiolytic and antidepressant effects of intracerebroventricularly administered somatostatin: behavioral and neurophysiological evidence. Neuroscience *157*, 666–676.

Fee, C., Prevot, T.D., Misquitta, K., Knutson, D.E., Li, G., Mondal, P., Cook, J.M., Banasr, M., and Sibille, E. (2021). Behavioral deficits induced by somatostatin-positive GABA neuron silencing are rescued by alpha 5 GABA-A receptor potentiation. Int. J. Neuropsychopharmacol. *24* (*6*), 505–518.

Florez, C.M., McGinn, R.J., Lukankin, V., Marwa, I., Sugumar, S., Dian, J., Hazrati, L.-N., Carlen, P.L., Zhang, L., and Valiante, T.A. (2015). In vitro recordings of human neocortical oscillations. Cereb. Cortex. *25*, 578–597.

Fuchs, T., Jefferson, S.J., Hooper, A., Yee, P.-H., Maguire, J., and Luscher, B. (2017). Disinhibition of somatostatin-positive GABAergic interneurons results in an anxiolytic and antidepressant-like brain state. Mol. Psychiatry *22*, 920–930.

Fuhrmann, G., Segev, I., Markram, H., and Tsodyks, M. (2002). Coding of temporal information by activity-dependent synapses. J. Neurophysiol. *87*, 140–148.

Gentet, L.J., Kremer, Y., Taniguchi, H., Huang, Z.J., Staiger, J.F., and Petersen, C.C.H. (2012). Unique functional properties of somatostatin-expressing GABAergic neurons in mouse barrel cortex. Nat. Neurosci. *15*, 607–612.

Gidon, A., Zolnik, T.A., Fidzinski, P., Bolduan, F., Papoutsi, A., Poirazi, P., Holtkamp, M., Vida, I., and Larkum, M.E. (2020). Dendritic action potentials and computation in human layer 2/3 cortical neurons. Science *367*, 83–87.

Gouwens, N.W., Berg, J., Feng, D., Sorensen, S.A., Zeng, H., Hawrylycz, M.J., Koch, C., and Arkhipov, A. (2018). Systematic generation of biophysically detailed models for diverse cortical neuron types. Nat. Commun. *9*, 710.

Grin-Yatsenko, V.A., Baas, I., Ponomarev, V.A., and Kropotov, J.D. (2009). EEG power spectra at early stages of depressive disorders. J. Clin. Neurophysiol. *26*, 401–406.

Guet-McCreight, A., and Skinner, F.K. (2019). Using computational models to predict in vivo synaptic inputs to interneuron specific 3 (IS3) cells of CA1 hippocampus that also allow their recruitment during rhythmic states. PLoS One *14*, e0209429.

Hagen, E., Næss, S., Ness, T.V., and Einevoll, G.T. (2018). Multimodal modeling of neural network activity: computing LFP, ECoG, EEG, and MEG signals with LFPy 2.0. Front. Neuroinform. *12*.

Halgren, M., Ulbert, I., Bastuji, H., Fabó, D., Erőss, L., Rey, M., Devinsky, O., Doyle, W.K., Mak-McCully, R., Halgren, E., et al. (2019). The generation and propagation of the human alpha rhythm. Proc Natl Acad Sci U S A *116*, 23772–23782.

Harris, J.A., Mihalas, S., Hirokawa, K.E., Whitesell, J.D., Choi, H., Bernard, A., Bohn, P., Caldejon, S., Casal, L., Cho, A., et al. (2019). Hierarchical organization of cortical and thalamic connectivity. Nature *575*, 195–202.

Den Hartog, H.M., Derix, M.M.A., Van Bemmel, A.L., Kremer, B., and Jolles, J. (2003). Cognitive functioning in young and middle-aged unmedicated out-patients with major depression: testing the effort and cognitive speed hypotheses. Psychol. Med. *33*, 1443–1451.

Hashemi, E., Ariza, J., Rogers, H., Noctor, S.C., and Martínez-Cerdeño, V. (2017). The number of parvalbumin-expressing interneurons is decreased in the prefrontal cortex in autism. Cereb. Cortex. *27*, 1931–1943.

Hashimoto, T., Volk, D.W., Eggan, S.M., Mirnics, K., Pierri, J.N., Sun, Z., Sampson, A.R., and Lewis, D.A. (2003). Gene expression deficits in a subclass of GABA neurons in the prefrontal cortex of subjects with schizophrenia. J. Neurosci. *23*, 6315–6326.

Hawrylycz, M.J., Lein, E.S., Guillozet-Bongaarts, A.L., Shen, E.H., Ng, L., Miller, J.A., van de Lagemaat, L.N., Smith, K.A., Ebbert, A., Riley, Z.L., et al. (2012). An anatomically comprehensive atlas of the adult human brain transcriptome. Nature *489*, 391–399.

Hay, E., and Segev, I. (2015). Dendritic excitability and gain control in recurrent cortical microcircuits. Cereb. Cortex. *25*, 3561–3571.

Hay, E., Hill, S., Schürmann, F., Markram, H., and Segev, I. (2011). Models of neocortical layer 5b pyramidal cells capturing a wide range of dendritic and perisomatic active properties. PLoS Comput. Biol. *7*, e1002107.

Hay, E., Schürmann, F., Markram, H., and Segev, I. (2013). Preserving axosomatic spiking features despite diverse dendritic morphology. J. Neurophysiol. *109*, 2972–2981.

Hodge, R.D., Bakken, T.E., Miller, J.A., Smith, K.A., Barkan, E.R., Graybuck, L.T., Close, J.L., Long, B., Johansen, N., Penn, O., et al. (2019). Conserved cell types with divergent features in human versus mouse cortex. Nature *573*, 61–68.

Holmes, W.R., and Rall, W. (1992). Estimating the electrotonic structure of neurons with compartmental models. J. Neurophysiol. *68*, 1438–1452.

Hu, X., Rocco, B.R., Fee, C., and Sibille, E. (2018). Cell type-specific gene expression of alpha 5 subunit-containing gamma-aminobutyric acid subtype A receptors in human and mouse frontal cortex. Mol Neuropsychiatry *4*, 204–215.

Huang, H., Thompson, W., and Paulus, M.P. (2017). Computational dysfunctions in anxiety: failure to differentiate signal from noise. Biol. Psychiatry *82*, 440–446.

Kang, H.J., Voleti, B., Hajszan, T., Rajkowska, G., Stockmeier, C.A., Licznerski, P., Lepack, A., Majik, M.S., Jeong, L.S., Banasr, M., et al. (2012). Decreased expression of synapse-related genes and loss of synapses in major depressive disorder. Nat. Med. *18*, 1413–1417.

Keller, A.J., Dipoppa, M., Roth, M.M., Caudill, M.S., Ingrosso, A., Miller, K.D., and Scanziani, M. (2020). A disinhibitory circuit for contextual modulation in primary visual cortex. Neuron *108*, 1181–1193.e8.

Khanahmadi, M., Malmir, M., Eskandari, H., and Orang, T. (2013). Evaluation of visual information processing speed in depressed people. Iran J. Public Health *42*, 1266–1273.

Koenigs, M., and Grafman, J. (2009). The functional neuroanatomy of depression: distinct roles for ventromedial and dorsolateral prefrontal cortex. Behav. Brain Res. *201*, 239–243.

Koetsier, G.C., Volkers, A.C., Tulen, J.H.M., Passchier, J., van den Broek, W.W., and Bruijn, J.A. (2002). CPT performance in major depressive disorder before and after treatment with imipramine or fluvoxamine. J. Psychiatr. Res. *36*, 391–397.

Komlósi, G., Molnár, G., Rózsa, M., Oláh, S., Barzó, P., and Tamás, G. (2012). Fluoxetine (prozac) and serotonin act on excitatory synaptic transmission to suppress single layer 2/3 pyramidal neuron-triggered cell assemblies in the human prefrontal cortex. J. Neurosci. *32*, 16369–16378.

Krienen, F.M., Goldman, M., Zhang, Q., C H Del Rosario, R., Florio, M., Machold, R., Saunders, A., Levandowski, K., Zaniewski, H., Schuman, B., et al. (2020). Innovations present in the primate interneuron repertoire. Nature *586*, 262–269.

Larkman, A.U. (1991). Dendritic morphology of pyramidal neurones of the visual cortex of the rat: III. Spine distributions. J. Comp. Neurol. *306*, 332–343.

Laubach, M., Amarante, L.M., Swanson, K., and White, S.R. (2018). What, if anything, is rodent prefrontal cortex? ENeuro *5* (*5*).

Lee, S., Hjerling-Leffler, J., Zagha, E., Fishell, G., and Rudy, B. (2010). The largest group of superficial neocortical GABAergic interneurons expresses ionotropic serotonin receptors. J. Neurosci. *30*, 16796–16808.

Levinson, A.J., Fitzgerald, P.B., Favalli, G., Blumberger, D.M., Daigle, M., and Daskalakis, Z.J. (2010). Evidence of cortical inhibitory deficits in major depressive disorder. Biol. Psychiatry *67*, 458–464.

Lewis, D.A., Hashimoto, T., and Volk, D.W. (2005). Cortical inhibitory neurons and schizophrenia. Nat. Rev. Neurosci. *6*, 312–324.

Lin, L.-C., and Sibille, E. (2013). Reduced brain somatostatin in mood disorders: a common pathophysiological substrate and drug target? Front. Pharmacol. *4*, 110.

Lin, L.C., and Sibille, E. (2015). Somatostatin, neuronal vulnerability and behavioral emotionality. Mol. Psychiatry *20*, 377–387.

Loken, C., Gruner, D., Groer, L., Peltier, R., Bunn, N., Craig, M., Henriques, T., Dempsey, J., Yu, C.-H., Chen, J., et al. (2010). SciNet: lessons learned from building a power-efficient top-20 system and data centre. J. Phys. Conf. Ser. *256*, 012026.

Ma, Y., Hu, H., Berrebi, A.S., Mathers, P.H., and Agmon, A. (2006). Distinct subtypes of somatostatin-containing neocortical interneurons revealed in transgenic mice. J. Neurosci. *26*, 5069–5082.

Mäki-Marttunen, T., Krull, F., Bettella, F., Hagen, E., Næss, S., Ness, T.V., Moberget, T., Elvsåshagen, T., Metzner, C., Devor, A., et al. (2019). Alterations in schizophrenia-associated genes can lead to increased power in delta oscillations. Cereb. Cortex. *29*, 875–891.

Marín, O. (2012). Interneuron dysfunction in psychiatric disorders. Nat. Rev. Neurosci. *13*, 107–120.

Markram, H., Muller, E., Ramaswamy, S., Reimann, M.W., Abdellah, M., Sanchez, C.A., Ailamaki, A., Alonso-Nanclares, L., Antille, N., Arsever, S., et al. (2015). Reconstruction and simulation of neocortical microcircuitry. Cell *163*, 456–492.

Martel, G., Dutar, P., Epelbaum, J., and Viollet, C. (2012). Somatostatinergic systems: an update on brain functions in normal and pathological aging. Front. Endocrinol. *3*, 154.

McDermott, L.M., and Ebmeier, K.P. (2009). A meta-analysis of depression severity and cognitive function. J. Affect. Disord. *119*, 1–8.

Miyata, S., Kumagaya, R., Kakizaki, T., Fujihara, K., Wakamatsu, K., and Yanagawa, Y. (2019). Loss of glutamate decarboxylase 67 in somatostatin-expressing neurons leads to anxiety-like behavior and alteration in the akt/GSK3β signaling pathway. Front. Behav. Neurosci. *13*, 131.

Mohan, H., Verhoog, M.B., Doreswamy, K.K., Eyal, G., Aardse, R., Lodder, B.N., Goriounova, N.A., Asamoah, B., B Brakspear, A.B.C., Groot, C., et al. (2015). Dendritic and axonal architecture of individual pyramidal neurons across layers of adult human neocortex. Cereb. Cortex. *25*, 4839–4853.

Molnár, G., Rózsa, M., Baka, J., Holderith, N., Barzó, P., Nusser, Z., and Tamás, G. (2016). Human pyramidal to interneuron synapses are mediated by multi-vesicular release and multiple docked vesicles. ELife *5*, e18167.

Moradi Chameh, H., Rich, S., Wang, L., Chen, F.-D., Zhang, L., Carlen, P.L., Tripathy, S.J., and Valiante, T.A. (2021). Diversity amongst human cortical pyramidal neurons revealed via their sag currents and frequency preferences. Nat. Commun. *12*, 2497.

Murray, J.D., Anticevic, A., Gancsos, M., Ichinose, M., Corlett, P.R., Krystal, J.H., and Wang, X.-J. (2014). Linking microcircuit dysfunction to cognitive impairment: effects of disinhibition associated with schizophrenia in a cortical working memory model. Cereb. Cortex. *24*, 859–872.

Northoff, G., and Sibille, E. (2014). Why are cortical GABA neurons relevant to internal focus in depression? A cross-level model linking cellular, biochemical and neural network findings. Mol. Psychiatry *19*, 966–977.

Obermayer, J., Heistek, T.S., Kerkhofs, A., Goriounova, N.A., Kroon, T., Baayen, J.C., Idema, S., Testa-Silva, G., Couey, J.J., and Mansvelder, H.D. (2018). Lateral inhibition by Martinotti interneurons is facilitated by cholinergic inputs in human and mouse neocortex. Nat. Commun. *9* (*1*), 4101.

Peng, Y., Mittermaier, F.X., Planert, H., Schneider, U.C., Alle, H., and Geiger, J.R.P. (2019). High-throughput microcircuit analysis of individual human brains through next-generation multineuron patch-clamp. ELife *8*, e48178.

Philip, N.S., Carpenter, L.L., Tyrka, A.R., and Price, L.H. (2010). Nicotinic acetylcholine receptors and depression: a review of the preclinical and clinical literature. Psychopharmacology *212*, 1–12.

Piantadosi, S.C., French, B.J., Poe, M.M., Timić, T., Marković, B.D., Pabba, M., Seney, M.L., Oh, H., Orser, B.A., Savić, M.M., et al. (2016). Sex-dependent anti-stress effect of an α5 subunit containing GABAA receptor positive allosteric modulator. Front. Pharmacol. *7*, 446.

Ponce, M., van Zon, R., Northrup, S., Gruner, D., Chen, J., Ertinaz, F., Fedoseev, A., Groer, L., Mao, F., Mundim, B.C., et al. (2019). Deploying a top-100 supercomputer for large parallel workloads: the niagara supercomputer. In Proceedings of the Practice and Experience in Advanced Research Computing on Rise of the Machines (Learning) (Association for Computing Machinery), pp. 1–8.

Prévot, T., and Sibille, E. (2020). Altered GABA-mediated information processing and cognitive dysfunctions in depression and other brain disorders. Mol. Psychiatry *26*, 151–167.

Prevot, T.D., Li, G., Vidojevic, A., Misquitta, K.A., Fee, C., Santrac, A., Knutson, D.E., Stephen, M.R., Kodali, R., Zahn, N.M., et al. (2019). Novel benzodiazepine-like ligands with various anxiolytic, antidepressant, or pro-cognitive profiles. Mol. Neuropsychiatry *5*, 84–97.

Prevot, T.D., Sumitomo, A., Tomoda, T., Knutson, D.E., Li, G., Mondal, P., Banasr, M., Cook, J.M., and Sibille, E. (2020). Reversal of age-related neuronal atrophy by α5-GABAA receptor positive allosteric modulation. Cereb. Cortex. *31* (*2*), 1395–1408.

Prönneke, A., Scheuer, B., Wagener, R.J., Möck, M., Witte, M., and Staiger, J.F. (2015). Characterizing VIP neurons in the barrel cortex of VIPcre/tdTomato mice reveals layer-specific differences. Cereb. Cortex. *25*, 4854–4868.

Ramaswamy, S., Courcol, J.-D., Abdellah, M., Adaszewski, S.R., Antille, N., Arsever, S., Atenekeng, G., Bilgili, A., Brukau, Y., Chalimourda, A., et al. (2015). The neocortical microcircuit collaboration portal: a resource for rat somatosensory cortex. Front. Neural Circuits *9* (*44*).

Schulz, J.M., Knoflach, F., Hernandez, M.-C., and Bischofberger, J. (2018). Dendrite-targeting interneurons control synaptic NMDA-receptor activation via nonlinear α5-GABAA receptors. Nat. Commun. *9*, 3576.

Scimemi, A., Andersson, A., Heeroma, J., Strandberg, J., Rydenhag, B., Mcevoy, A., Thom, M., Asztely, F., and Walker, M. (2006). Tonic GABAA receptor-mediated currents in human brain. Eur. J. Neurosci. *24*, 1157–1160.

Seeman, S.C., Campagnola, L., Davoudian, P.A., Hoggarth, A., Hage, T.A., Bosma-Moody, A., Baker, C.A., Lee, J.H., Mihalas, S., Teeter, C., et al. (2018). Sparse recurrent excitatory connectivity in the microcircuit of the adult mouse and human cortex. ELife *7*, e37349.

Seney, M.L., Tripp, A., McCune, S., Lewis, D., and Sibille, E. (2015). Laminar and cellular analyses of reduced somatostatin gene expression in the subgenual anterior cingulate cortex in major depression. Neurobiol. Dis. *73*, 213–219.

Sibille, E. (2017). Reduced somatostatin expression or somatostatin-positive gamma-aminobutyric acid neurons: a shared pathology across brain disorders. Biol. Psychiatry *81*, 467–469.

Silberberg, G., and Markram, H. (2007). Disynaptic inhibition between neocortical pyramidal cells mediated by martinotti cells. Neuron *53*, 735–746.

Sivagnanam, S., Majumdar, A., Yoshimoto, K., Astakhov, V., Bandrowski, A., Martone, M., and Carnevale, N. (2013). Introducing the neuroscience gateway. CEUR Workshop Proc. *993*.

Song, X.M., Hu, X.-W., Li, Z., Gao, Y., Ju, X., Liu, D.-Y., Wang, Q.-N., Xue, C., Cai, Y.-C., Bai, R., et al. (2021). Reduction of higher-order occipital GABA and impaired visual perception in acute major depressive disorder. Mol. Psychiatry, 1–9.

Szegedi, V., Paizs, M., Csakvari, E., Molnar, G., Barzo, P., Tamas, G., and Lamsa, K. (2016). Plasticity in single axon glutamatergic connection to GABAergic interneurons regulates complex events in the human neocortex. PLoS Biol. *14* (*11*).

Taylor Tavares, J.V., Clark, L., Cannon, D.M., Erickson, K., Drevets, W.C., and Sahakian, B.J. (2007). Distinct profiles of neurocognitive function in unmedicated unipolar depression and bipolar II depression. Biol. Psychiatry *62*, 917–924.

Teleńczuk, B., Dehghani, N., Le Van Quyen, M., Cash, S.S., Halgren, E., Hatsopoulos, N.G., and Destexhe, A. (2017). Local field potentials primarily reflect inhibitory neuron activity in human and monkey cortex. Sci. Rep. *7*, 40211.

Tremblay, R., Lee, S., and Rudy, B. (2016). GABAergic interneurons in the neocortex: from cellular properties to circuits. Neuron *91*, 260–292.

Tsourtos, G., Thompson, J.C., and Stough, C. (2002). Evidence of an early information processing speed deficit in unipolar major depression. Psychol. Med. *32*, 259–265.

Van Geit, W., Gevaert, M., Chindemi, G., Rössert, C., Courcol, J.-D., Muller, E.B., Schürmann, F., Segev, I., and Markram, H. (2016). BluePyOpt: leveraging open source software and cloud infrastructure to optimise model parameters in neuroscience. Front. Neuroinform. *10* (*17*).

Welch, P. (1967). The use of fast Fourier transform for the estimation of power spectra: a method based on time averaging over short, modified periodograms. IEEE Trans. Audio Electroacoustics *15*, 70–73.

Xue, M., Atallah, B.V., and Scanziani, M. (2014). Equalizing excitation-inhibition ratios across visual cortical neurons. Nature *511*, 596–600.

Yu, J., Hu, H., Agmon, A., and Svoboda, K. (2019). Recruitment of GABAergic interneurons in the barrel cortex during active tactile behavior. Neuron *104*, 412–427.e4.

Zurita, H., Feyen, P.L.C., and Apicella, A.J. (2018). Layer 5 callosal parvalbumin-expressing neurons: a distinct functional group of GABAergic neurons. Front. Cell. Neurosci. *12*, 53.

STAR★METHODS

KEY RESOURCES TABLE

REAGENT or RESOURCE	SOURCE	IDENTIFIER
Software and algorithms		
Python 3.7	Python Software Foundation	https://www.python.org/
BluePyOpt	Van Geit et al., 2016	https://github.com/BlueBrain/BluePyOpt
NEURON 7.7	Carnevale and Hines, 2006	https://neuron.yale.edu/neuron/
LFPy	Hagen et al., 2018	https://lfpy.readthedocs.io/en/latest/#
Multiple Objective Evolutionary Algorithm	Hay et al. 2011	https://journals.plos.org/ploscompbiol/article?id=10.1371/journal.pcbi.1002107
Human L2/3 microcircuits models and simulation code	This paper	https://doi.org/10.5281/zenodo.5771000

RESOURCE AVAILABILITY

Lead contact

Further information and requests for resources should be directed to and will be fulfilled by the lead contact, Etay Hay (etay.hay@camh.ca).

Materials availability

This study did not generate new unique reagents

Data and code availability

- Simulation data reported in this paper will be shared by the lead contact upon request.
- All original code has been deposited at Zenodo and is publicly available as of the date of publication. DOIs are listed in the key resources table.
- Any additional information required to reanalyze the data reported in this paper is available from the lead contact upon request.

EXPERIMENTAL MODEL AND SUBJECT DETAILS

We used whole-cell recordings from human medial temporal gyrus, L2/3 Pyr neurons (Moradi Chameh et al., 2021) (n = 28 neurons, 9 neurons from 3 male subjects and 19 neurons from 5 female subjects), and putative SST (Neuron ID: 571700636), PV (Neuron ID: 529807751) and VIP (Neuron ID: 525018757) interneurons available from the Allen Brain Atlas (Hawrylycz et al., 2012; Allen Institute for Brain Science, 2010). We used reconstructed human neuron morphologies from the Allen Brain Atlas for a Pyr neuron (Neuron ID: 531526539) and the above three interneurons.

In addition, we used current recordings of tonic inhibition in human cortical L2/3 Pyr neurons (10 cells: 9 cells from 3 male subjects, 1 cell from 1 female subject). Written informed consent was obtained from all participants, in accordance with the Declaration of Helsinki and the University Health Network Research Ethics board.

METHOD DETAILS

Human L2/3 microcircuit models

We simulated cortical L2/3 microcircuits comprised of 1000 neurons distributed along a 500x500x950 μm^3 volume (250 to 1200 μm below pia, spanning L2/3 (Mohan et al., 2015)) using NEURON (Carnevale and Hines, 2006) and LFPy (Hagen et al., 2018). We used human data to constrain the models where available (Table S1 and see below). Neurons of a given type had the same model (morphology and biophysical properties, see below) but differed in synaptic connectivity and background input (see below). The proportions of the four neuron types in the microcircuit were: 80% Pyr, 5% SST, 7% PV, and 8% VIP, according to the relative neuron densities found in the rodent and human cortical L2/3 in previous studies (Hashemi et al., 2017; Krienen et al., 2020), and RNA-seq data from the Allen Human Brain Atlas (Hodge et al., 2019).

Neuron models

We derived multi-compartmental conductance-based models for the different neuron types using multi-objective optimization with a genetic algorithm from previous in-house code (Hay et al., 2011) for optimizing the Pyr and SST neuron models, and the BluePyOpt Python module (Van Geit et al., 2016) for optimizing the PV and VIP neuron models. We used a set of ion channel mechanisms taken unchanged from previously published models(Hay et al., 2011, 2013). We used five hyperpolarizing and depolarizing current steps from the electrophysiological data for model optimizations (Tables S2–S5). Three depolarizing supra-threshold current steps were used for targeting appropriate firing features at low, medium and high firing rates. A small hyperpolarizing step current was used for fitting passive features, and a large hyperpolarizing current step was used for fitting sag voltage. Pyr and SST neuron models were fitted using a two-step process, where first h-current and passive parameters ($\overline{g}_H$, $\overline{g}_{Leak}$,) were fitted to capture passive and sag voltage features during hyperpolarizing current steps, and then other ion channel parameters ($\overline{g}_{Na}$, $\overline{g}_K$, $\overline{g}_{Ca}$) were fitted to capture spiking features during depolarizing current steps (Tables S2 and S3). The PV and VIP neuron models were fitted in one step where passive and firing features were optimized simultaneously (Tables S4 and S5). For all models, R_a = 100 Ω cm, E_{Na} = 50 mV, E_K = -85 mV, and $CaDynamics_{gamma}$ = 0.0005 (Hay et al., 2011). Axonal Na_T kinetics parameters were $Vshift_m$ = 0, $Vshift_h$ = 10, $Slope_m$ = 9, and $Slope_h$ = 6 for all models (Hay et al., 2011, 2013). For somatic Na_T kinetics, $Vshift_m$ = 13, $Vshift_h$ = 15, $Slope_m$ = 7, and $Slope_h$ = 6 (Hay et al., 2011, 2013), except for the PV neuron model where these parameters at the soma were the same as in the axon to compensate for reduced action potential propagation brought on by the axon replacement method. The specific membrane capacitance (c_m) was 1 μF/cm^2, and 2 μF/cm^2 in the dendrites to compensate for spine area loss in Pyr neuron reconstructions (Holmes and Rall, 1992; Larkman, 1991) or where required to reproduce membrane time constants in interneurons, possibly due to errors in dendritic diameter estimation (Table S6). $\overline{g}_H$ was distributed uniformly across all dendritic sections, with the exception of Pyr apical dendrites which followed an exponential increase with distance from soma as follows:

$$\overline{g}_H = \overline{g}_{H,\,soma}(-0.8696 + 2.0870\exp(3.6161(X_{relative}))) \quad \text{(Equation 1)}$$

where $X_{relative}$ is the relative distance from soma to maximal length (i.e. from 0 to 1) (Hay et al., 2011). Model optimization was run using parallel computing clusters (SciNet (Loken et al., 2010; Ponce et al., 2019): 400 processors with a population size of 1000, for 1000 generations and an approximate total runtime of 2 hours; Neuroscience Gateway, NSG (Sivagnanam et al., 2013): 400 processors with a population size of 400, for 300 generations and an approximate total runtime of 5 hours). Model performance in reproducing the electrophysiological features was assessed in terms of standard deviation from the experimental mean. For Pyr neuron models we used the statistics over the set of recorded neurons (see above). For the interneurons, where only a single human neuron was clearly identified for each neuron type, we used the values of the human neuron with population variance from the rodent literature (Ma et al., 2006; Prönneke et al., 2015; Zurita et al., 2018).

Synaptic connectivity models

Where possible, we constrained synaptic parameters using the human experimental literature. Otherwise, we used parameters from the rodent literature (the Blue Brain Project (Ramaswamy et al., 2015)). We used previous models of NMDA/AMPA excitatory and $GABA_A$ inhibitory synapses, that incorporated presynaptic short-term plasticity parameters for vesicle-usage, facilitation, and depression, as well as separate time constant parameters for the AMPA and NMDA components of excitatory synapses (Fuhrmann et al., 2002; Hay and Segev, 2015; Mäki-Marttunen et al., 2019). We set the same time constant parameters for all connection types ($\tau_{rise,NMDA}$ = 2 ms; $\tau_{decay,NMDA}$ = 65 ms; $\tau_{rise,AMPA}$ = 0.3 ms; $\tau_{decay,AMPA}$ = 3 ms; $\tau_{rise,GABA}$ = 1 ms; $\tau_{decay,GABA}$ = 10 ms), as well as the reversal potential values (E_{exc} = 0 mV; E_{inh} = -80 mV).

We fitted the synaptic conductance, and vesicle usage parameters (Hay and Segev, 2015) where available, using the human experimental literature for most of the key connection types: Pyr→Pyr connections (Seeman et al., 2018), Pyr→SST connections and SST→Pyr connections (Obermayer et al., 2018), PV→Pyr connections (Komlósi et al., 2012), and Pyr→PV connections (Szegedi et al., 2016). We simulated the experimental conditions (e.g., chloride reversal potential, and holding currents) and adjusted the conductance and vesicle usage parameters to achieve the target postsynaptic amplitudes and failure rates on average across 200 randomizations of synaptic locations and events. For the conductance and vesicle usage parameters of all other connection types, as well as the depression, facilitation, and numbers of synaptic contacts for all connections, we used model parameters reported for rodents by the Blue Brain Project (Markram et al., 2015; Ramaswamy et al., 2015). The synaptic parameters of the different connections are summarized in Table S7. Synaptic locations onto Pyr neurons were random but depended on the connection type, where Pyr→Pyr synapses were placed on both basal and apical dendritic compartments, PV→Pyr connections were placed on basal dendritic compartments, and SST→Pyr connections were placed on apical dendritic compartments. Apart from these specifications, synapse locations were chosen randomly from a uniform distribution.

We set unidirectional connection probability (p_{con}) according to the rodent literature (Blue Brain Project and Allen Brain Institute), except for Pyr→Pyr connections, where p_{con} was set to 15% according to the human literature (Seeman et al., 2018). We adjusted some connection probabilities guided by the reported experimental ranges to reproduce the intrinsic activity in the microcircuit (see below). The connection probabilities in the microcircuit are summarized in Table S7.

Tonic inhibition recordings data

The data was collected using surgery resection, solutions, tissue preparation, and recording equipment described previously (Moradi Chameh et al., 2021). Neocortical tissue resected during tumor resection and anterior temporal lobectomy was immediately submerged in ice-cold cutting solution and transferred to a recording chamber within 20 minutes. After sectioning the tissue, the slices were incubated for 30 min at 34 °C in standard artificial cerebrospinal fluid (aCSF) (in mM): NaCl 123, KCl 4, CaCl2.2H2O 1, MgSO4.7H2O 1, NaHCO3 26, NaH2PO4.H2O 1.2, and D-glucose 10, pH 7.40 and bubbled with carbogen gas. Whole-cell patch-clamp recordings were obtained using a Multiclamp 700 A amplifier, Axopatch 200B amplifier, and pClamp 9.2 and pClamp 10.6 data acquisition software (Axon instruments, Molecular Devices, USA). Subsequently, electrical signals were digitized at 20 kHz using a 1320X digitizer. For voltage-clamp recordings of tonic current, low-resistance patch pipettes (2 – 4 MΩ) were filled with a CsCl-based solution containing (in mM) 140 CsCl, 10 EGTA, 10 Hepes, 2 MgCl2, 2 Na2ATP, 0.3 GTP, and 5 QX314 adjusted to pH 7.3 with CsOH. Experiments were performed with excitatory (APV 25 μM, Sigma; CNQX 10 μM, Sigma) and GABAB (CGP-35348 10 μM, Sigma) synaptic activity blocked as in previous studies (Asgari et al., 2016; Schulz et al., 2018). The junction potential was calculated to be 4.3 mV and the holding potential was -74.3 mV after junction potential correction. Mean amplitude of baseline tonic current in presence of GABA (5 μM) and glutamatergic blocker was 65.8 ± 10.2 pA (n = 10 cells).

Tonic inhibition models

We modelled tonic inhibition using a model for outward rectifying tonic inhibition (Bryson et al., 2020) and estimated the conductance of tonic inhibition (G_{tonic}; uniformly across all somatic, basal, and apical compartments) using current magnitude in human cortical L2/3 Pyr neurons (see above), which agreed with values from the human layer 5/6 literature (Scimemi et al., 2006). We replicated the experimental conditions by setting the GABA reversal potential to -5 mV (i.e. consistent with a high chloride intracellular solution), setting the holding potential to -75 mV in voltage-clamp mode, and reproduced the target tonic inhibition current amplitude with G_{tonic}: 0.938 mS/cm^2. We used the same value for the interneurons since the total tonic inhibition current recorded in interneurons was similar to that of Pyr neurons after correcting for cell capacitance (Scimemi et al., 2006).

Modelling microcircuit baseline and response activity

We constrained the microcircuit to generate spike rates at baseline and during response (see below) as reported for the different neuron types *in vivo*. For baseline activity of Pyr neurons, we used values recorded in humans and monkeys *in vivo* (Teleńczuk et al., 2017) (Subject 1: 0.66 ± 0.51 Hz; Subject 2: 0.32 ± 0.38 Hz; Monkey: 1.31 ± 1.11 Hz), and for baseline activity of the interneuron types we used values recorded in rodents *in vivo* (SST: 6.3 ± 0.6 Hz; PV: 9.4 ± 2.1 Hz; VIP: 3.7 ± 0.7 Hz) (Gentet et al., 2012; Yu et al., 2019). We note that baseline Pyr rates in human and rodents in the above studies were largely similar. We reproduced the baseline firing rates by adjusting the connection probability values guided by the reported experimental ranges (see above) for all connection types except Pyr→Pyr connections, and by adjusting the background input (see below). We calculated the simulated rates across non-silent neurons (> 0.2 Hz), as in the above experimental studies. We further constrained the microcircuit model to reproduce a doubling of baseline Pyr neuron spike rates when SST interneurons were silenced, as seen experimentally (Gentet et al., 2012) (baseline: 1.2 ± 0.2 Hz; SST interneurons silenced: 2.2 ± 0.3 Hz).

The microcircuit received random background excitatory input using Ornstein-Uhlenbeck (OU) point processes (Destexhe et al., 2001), placed at halfway the length of each dendritic arbor to ensure similar levels of inputs along each dendritic path to the soma. For the Pyr neuron models, we placed 5 additional OU processes along the apical trunk at 10%, 30%, 50%, 70%, and 90% of the apical dendritic length. We set the base excitatory OU conductances to the following: Pyr = 28 pS; SST = 30 pS; PV = 280 pS; VIP = 66 pS. We set the inhibitory OU conductance to 0, since the model microcircuit provided sufficient inhibition. Furthermore, we scaled the OU conductance values to increase with distance from soma by multiplying them with the exponent of the relative distance from soma (ranging from 0 to 1): $\bar{g}_{OU} = \bar{g} \times \exp(X_{relative})$.

We modelled the spike response rates and profiles using values recorded in the different neuron types *in vivo*, in behaving rodents (Gentet et al., 2012) (change in firing rate compared to pre-stimulus rate: Pyr 2.2 ± 1.0 Hz, SST: -2.9 ± 0.9 Hz; PV: 21.8 ± 8.9 Hz; VIP: 14.0 ± 3.0 Hz). We reproduced the response rates by synaptic stimulation of the model microcircuits representing a bottom-up (thalamic) input. We tuned the microcircuit connectivity, the stimulus input conductance and stimulus timing in the different neuron types to reproduce the experimental response profiles and timing of activation (Gentet et al., 2012; Yu et al., 2019). The model neurons were stimulated using excitatory AMPA/NMDA synapses with the same synaptic dynamics and number of contacts as the cortical excitatory synapses above. 55 Pyr neurons were stimulated in the basal dendrites, with 2 – 4 ms delay post-stimulus and a conductance of 4 nS. 35 PV interneurons were stimulated with a delay of 2 - 2.5 ms and a conductance of 2 nS. VIP interneurons were stimulated in two groups and phases: early (65 VIP interneurons, delay = 0.5 - 4.5 ms, conductance = 2.8 nS) and late (80 VIP interneurons, delay = 7 - 12 ms, conductance = 2.2 nS). This stimulus paradigm was applied to 200 randomized healthy and depression microcircuits. Average pre-stimulus rates were calculated over the 2 seconds before stimulus onset. Average post-stimulus rates were calculated over the 5 - 55 ms window after stimulus onset. To examine and visualize the stimulus response in each of the four cell types, we calculated peristimulus time histograms of the spike counts of non-silent cells (> 0.2 Hz) in 10 ms bins, 200 ms before and after stimulus, pooled across 200 randomized microcircuits. We also tested apical dendritic stimulation, with parameters as above except that the input synapses were distributed on the apical dendrites instead of the basal dendrites, and the stimulated Pyr neuron population size was 85 neurons.

Spikes PSD

Power spectral density (PSD) of Pyr neuron population spiking during baseline microcircuit activity was computed by first converting the spike times into binary spike train vectors and then summing the binary spike train vectors across all Pyr neurons. PSD was then computed from the summed spike train vectors using Welch's method (Guet-McCreight and Skinner, 2019; Welch, 1967) from the SciPy python module (nperseg=100,000 sampling points, equivalent to 2.5s time windows). PSD vectors across random seeds were then bootstrapped at each frequency 500 times, from which the resulting bootstrapped means and 95% confidence intervals were computed.

Human depression microcircuit models

We modelled depression microcircuits by reducing the conductance of SST interneuron synaptic and tonic inhibition on all cell types by 40%, as indicated by the 40% reduction of SST expression in SST interneurons in L2/3 in post-mortem brain tissue of patients with depression (Seney et al., 2015). For Pyr neurons, we selectively decreased the tonic inhibition by 40% in the apical dendrites. For each interneuron, we estimated the relative contribution of SST interneurons to the total inhibitory input and reduced the tonic inhibition by 40% of the relative contribution. This relative contribution was calculated by multiplying the SST synaptic conductance, connection probability, and the number of contacts, and dividing by the summed contributions of all interneuron types.

False/failed signal detection rates

We calculated the error rates in stimulus processing by first computing the distribution of pre-stimulus firing rates of all Pyr neurons per circuit run (sliding windows of 50 ms over 2 seconds pre-stimulus, windows sliding in 1 ms steps for a total of 1950 windows), and the distribution of post-stimulus spike rates of all Pyr neurons (in the 5 – 55 ms window post stimulus) across 200 randomized microcircuits. The intersection point between the two distributions was set as the stimulus detection threshold. The probability of false detection was calculated by the integral of the pre-stimulus distribution above the detection threshold divided by the integral of the entire pre-stimulus distribution. The probability of failed detection was calculated by the integral of the post-stimulus distribution below the detection threshold divided by the integral of the entire post-stimulus distribution.

QUANTIFICATION AND STATISTICAL ANALYSIS

We determined statistical significance using paired-sample or two-sample t test ($p < 0.05$), where appropriate. We calculated the effect size using Cohen's *d* (the difference in means divided by the pooled standard deviation). For each condition, n = 200 circuits were simulated.